Effects of Disorder on Carrier Transport in Cu_2SnS_3

Lauryn L. Baranowski,[1,2] Kevin McLaughlin,[2] Pawel Zawadzki,[1] Stephan Lany,[1] Andrew Norman,[1] Hannes Hempel,[3] Rainer Eichberger,[3] Thomas Unold,[3] Eric S. Toberer,[1,2] and Andriy Zakutayev[1,*]

[1]*National Renewable Energy Laboratory, 15013 Denver West Parkway, Golden, Colorado 80401, USA*
[2]*Physics Department, Colorado School of Mines, 1500 Illinois Street, Golden, Colorado 80401, USA*
[3]*Helmholtz Zentrum Berlin für Materialien und Energie GmbH, Hahn Meitner Platz 1, 14109 Berlin, Germany*

(Received 6 April 2015; revised manuscript received 3 September 2015; published 28 October 2015)

Cu_2SnS_3 is a promising absorber material that has attracted significant interest in recent years. However, similar to $Cu_2ZnSn(S,Se)_4$ (CZTS), Cu_2SnS_3 displays cation disorder, which complicates the scientific understanding and technological applications of these materials. In this work, we use postdeposition annealing to convert disordered Cu_2SnS_3 thin films to the ordered structure. After annealing, we observe crystal structure changes and detect improvements in the majority carrier (hole) transport. However, when the minority carrier (electron) transport is investigated by using optical-pump terahertz-probe spectroscopy, minimal differences are observed in the lifetimes of the photoexcited charge carriers in the ordered and disordered Cu_2SnS_3. By combining the experimental data with theoretical results from first-principles calculations and Monte Carlo simulations, we are able to conclude that even ostensibly "ordered" Cu_2SnS_3 displays minority carrier transport properties corresponding to the disordered structure. Transmission electron microscopy investigations reveal only a very low density of planar defects (stacking faults and/or twins) in the annealed film, suggesting that these imperfections can dominate minority carrier transport even at low levels. The results of this study highlight some of the challenges in the development of Cu_2SnS_3-based photovoltaics and have implications for other disordered multinary semiconductors such as CZTS.

DOI: 10.1103/PhysRevApplied.4.044017

I. INTRODUCTION

The development of efficient and scalable photovoltaics is an important challenge in today's energy landscape. Although highly efficient thin-film photovoltaics have been commercially available for some time, these technologies may be limited in their scalability by the use of rare or toxic elements [1–3]. Cu_2SnS_3 is a promising thin-film photovoltaic absorber material which uses only abundant and nontoxic elements. Interest in this compound has rapidly increased in the past several years, and device efficiencies of 4% and 6% have been reported using Cu_2SnS_3-based absorber materials and alloys, respectively [4,5].

Besides the reported device efficiencies, previous theoretical and experimental works have revealed promising attributes of Cu_2SnS_3 for photovoltaic absorber applications. First-principles calculations show a wide range of phase stability, high optical absorption coefficient, and lack of Fermi-level pinning in this material [6]. Experimental reports of the band gap of Cu_2SnS_3 range from 0.9 to 1.35 eV, well suited for a single-junction photovoltaic device [7,8]. Furthermore, band gap tuning can be achieved either by alloying with Si or Ge on the Sn site (increasing band gap) or with Se on the S site (decreasing band gap) [5,9,10]. Research demonstrates that Cu_2SnS_3 can be synthesized by several potentially scalable techniques such as sputtering and solution processing [5,11,12].

A variety of crystal structures are reported for Cu_2SnS_3 thin films, including cubic, tetragonal, monoclinic, and triclinic [5,12,13]. These varying crystal structures result from different degrees of Cu/Sn disorder on the cation sites of the zinc-blende-based lattice (see Fig. S2 [14]) [15]. A recent theoretical work suggests that this disorder takes the form of compositional inhomogeneities caused by entropy-driven clustering (rather than fully random cation disorder) and could lead to nanoscale potential fluctuations that negatively affect the carrier transport in Cu_2SnS_3 [16]. It has been demonstrated that annealing Cu_2SnS_3 thin films at higher temperatures promotes a transformation from the tetragonal to the monoclinic structure [17]. A few other studies consider annealing of Cu_2SnS_3, including an investigation of the behavior of extrinsic oxygen defects in this material [18]. However, there has been no work on the behavior of intrinsic defects during the annealing process or the effects of annealing on the electronic properties of Cu_2SnS_3.

The reported hole concentrations in Cu_2SnS_3 are often high, reaching 10^{20} cm^{-3} in some reports [19,20]. This level of doping is generally considered too high for a photovoltaic absorber material, as it leads to a tunneling-enhanced increase in recombination within the absorber layer and at the heterojunction interface, and is unfavorable

*Corresponding author.
andriy.zakutayev@nrel.gov

in polycrystalline films due to a short depletion width. In our prior work, we determined that two mechanisms control the doping in Cu_2SnS_3 [21]. First, films must be grown Cu poor to avoid alloying with a metallic Cu_3SnS_4 phase. Second, the S chemical potential during film growth controls the concentration of Cu vacancies, which are the dominant acceptor defect. Using the chemical-potential phase space for this system [6], we determine that the lowest Cu and S chemical potentials are found when Cu_2SnS_3 is on the phase boundary with SnS (but without SnS impurities). Thus, film growth in this region of the phase space should lead to the desired carrier concentrations on the order of $10^{17}cm^{-3}$.

In this work, we anneal our as-deposited Cu_2SnS_3 films under an SnS atmosphere. We find that this annealing causes a transformation from the cubic or tetragonal structure to the monoclinic structure (corresponding to an increase in cation ordering), along with a decrease in the hole concentration and an increase in the hole mobility. We use optical-pump terahertz-probe spectroscopy to investigate the minority carrier transport in our Cu_2SnS_3 films. Despite significant differences in cation ordering, both samples have short electron decay times on the order of 0.1–10 ps and similarly high degrees of charge localization. From the electronic structure calculations, these short decay times and high degree of charge localization are characteristic of a disordered structure. When the samples are imaged with transmission electron microscopy, the cubic film is found to have a high density of planar defects (stacking faults and/or twins). In contrast, only a small fraction of grains in the monoclinic film show planar defects. We conclude that, even when most of the planar defects are eliminated through annealing, these imperfections still dominate the minority-charge-carrier transport. The findings in this work have implications not only for Cu_2SnS_3, but also for $Cu_2ZnSn(S,Se)_4$ (CZTS) and other multinary disordered semiconductors.

II. METHODS

A. Initial film growth and annealing

The films described in this paper are deposited by using combinatorial rf sputtering from 50-mm-diameter Cu_2S and SnS_2 targets on heated 50×50 mm Eagle XG glass substrates, under conditions described in Ref. [21]. We note that, after sputter deposition, the films are already in the Cu_2SnS_3 phase, which is different from many other studies, in which metal precursors are deposited and annealed to form the final ternary phase. Eagle XG glass is chosen for its low Na content, so that Na diffusion during film growth or annealing will not affect the measured transport properties. Further information about combinatorial synthesis approaches as applied to other absorber materials can be found in Refs. [22–25].

Annealing is performed by placing the samples in a quartz tube along with approximately 1 g of SnS or SnS_2 powder in an alumina boat (details regarding the synthesis of the SnS and SnS_2 powders can be found in Supplemental Material [14]). A thermocouple is inserted into the tube such that it is positioned directly over the sample. A constant flow of argon gas is supplied to the quartz tube and exits via a bubbler filled with mineral oil (pressure within the tube is assumed to be close to atmospheric). The samples are heated in a tube furnace with a 5-h total ramp time to the desired temperature. After the desired hold time, the furnace is turned off and allowed to cool naturally to room temperature. A diagram of the annealing setup can be found in Supplemental Material (Fig. S1) [14].

B. Film characterization

Characterization is performed on small (12.5 mm × 12.5 mm) sections of the original films, which are determined to be uniform with regards to composition and morphology (due to the shallow initial compositional gradient and size of the film sections). X-ray fluorescence (XRF) spectra are collected by using a Fischer XDV-SDD instrument to obtain both the Cu/Sn ratios and the thickness of the films. A table of these data can be found in Supplemental Material [14]. The XRF is calibrated with approximately 20 elemental standards from Fischer that span the entire energy range of the XRF measurement. The x-ray diffraction patterns are collected by using a $\theta - 2\theta$ geometry with Cu $K\alpha$ radiation and a proportional 2D detector (Bruker D8 Discover with General Area Detector Diffraction System software). Raman spectra are collected by using a Renishaw inVia confocal Raman microscope configured with 532-nm laser excitation at 5% power, an 1800-mm^{-1} grating, and a CCD array detector. To compensate for the small spot size of the Raman measurement (approximately 10 μm), six measurements are taken on each sample and averaged to provide a final spectrum.

Room-temperature Hall measurements (BioRad HL5500 PC) are used to determine carrier concentration and majority carrier mobility. Room-temperature Hall measurements are attempted on all annealed samples; however, for some samples, the Hall voltages are within the noise of the instrument, and thus the data are not valid. We find that all samples annealed in the SnS atmosphere (for which successful Hall measurements are performed) have carrier mobilities ranging from 2 to 5 $cm^2/V\,s$; the average value is 2.5 $cm^2/V\,s$. This value of mobility, combined with the electrical conductivity, is used to calculate the carrier concentration for samples that are not successfully measured by using the Hall effect. The p-type electrical conduction is confirmed by measuring the Seebeck coefficient on a home-built system. Transmission electron microscopy (TEM) cross-section samples are prepared by using a conventional focused ion beam (FIB) liftout technique and examined at 300 kV in an FEI Tecnai G2 30 S-TWIN TEM.

We use optical-pump terahertz-probe spectroscopy (OPTP), also known as time-resolved terahertz spectroscopy, to measure the decay of pump-induced conductivity in the picosecond range as well as the complex charge-carrier mobility. The OPTP spectrometer has been described earlier [26]. The setup has been modified recently to record the pump-induced change in the terahertz reflection configuration. The transients are measured at the point of maximum change in terahertz amplitude, which represents the averaged terahertz conductivity decay, while the mobilities are analyzed by fitting the recorded terahertz reflection spectra to an optical model by using the transfer-matrix method [27]. We assume that the decay in conductivity is caused by a decaying carrier concentration where the maximum of the transient corresponds to all initially induced carriers. While the measured mobility is an average over all excited charge carriers, the conductivity is dominated by the electron (minority carrier) properties if the electron mobility can be assumed to be larger than the hole mobility [28].

C. Computational methods

The density of states (DOS) and projected density of states are calculated by using the VASP code [29]. Because of the band gap problem of the semilocal density functional theory (DFT) and large cells necessary to describe disorder in Cu_2SnS_3, we perform non-self-consistent Heyd-Scuseria-Ernzerhof (HSE) calculations [30]. The wave functions for HSE are generated with DFT + U [31] using a Perdew-Burke-Ernzerhof [32,33] exchange-correlation functional and on-site potential $U = 7$ eV applied to Cu(d) states.

To compare the degree of charge localization in the ordered (SG = Cc) and disordered Cu_2SnS_3, we also calculate the inverse participation ratio (IPR). The IPR measures the inverse of the fraction of atoms over which a given state is delocalized and takes the form

$$\mathrm{IPR} = \frac{N\sum_i^N c_i^4}{(\sum_i^N c_i^2)^2}, \qquad (1)$$

where the sums run over N atoms in the unit cell and c_i are atom-projected density of states. For instance, for a state that is delocalized over all atoms in the unit cell, IPR = 1; for a state delocalized over half of the atoms in the unit cell, IPR = 2.

For the disordered Cu_2SnS_3, the DOS and IPR are averaged over four independent atomic structures generated by using the Metropolis Monte Carlo method with a local motif-based model Hamiltonian described in Ref. [16].

III. RESULTS AND DISCUSSION

We investigate a variety of annealing conditions to determine their effects on the transport properties of Cu_2SnS_3. The annealing temperature, atmosphere, and duration are independently explored to determine the effects on the carrier concentration, and these results are presented in Fig. 1. As expected from the chemical-potential phase space, the lowest hole concentrations are achieved under an SnS/Ar atmosphere (square data points in Fig. 1) [21]. Comparing the results for 30 min, 2 h, and 8 h (red, blue, and green data points, respectively), we find that the kinetics of the annealing process are relatively slow. Further discussion of these results can be found in Supplemental Material [14]. As a representative sample, we select the film that is annealed under an SnS/Ar atmosphere at 500° for 2 h. All further results presented in this work are taken from this sample, and are summarized in Table I.

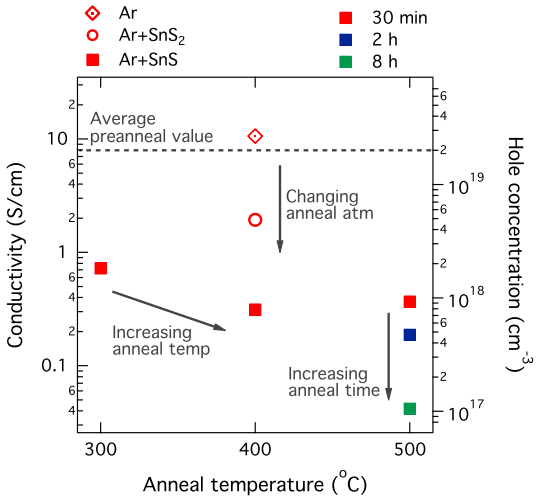

FIG. 1. As expected from the Cu-Sn-S chemical-potential phase space, carrier concentration reductions are largest when the Cu_2SnS_3 films are annealed in equilibrium with SnS (square markers). Increasing the anneal temperature shows some effect on the hole concentration; increasing the anneal time causes more dramatic reductions. The preanneal values of carrier concentration are approximately 2×10^{19} cm^{-3}.

A. Structural changes and majority carrier transport

We assess changes in the crystal structure of the Cu_2SnS_3 films by using x-ray diffraction (XRD) and Raman spectroscopy. Overall, we see a change from a primarily cubic as-deposited structure to a monoclinic postannealed structure. This indicates a change from a disordered cation sublattice (cubic or tetragonal) to an ordered sublattice (monoclinic). For more information and figures of these structures, see Fig. S2 in Supplemental Material [14].

Prior to annealing, the XRD pattern displays only one peak at approximately 28.5°, shown in Fig. 2(a). With only this peak, it is difficult to assign a definitive crystal structure to this XRD pattern: This peak could correspond to the cubic (PDF No. 04-002-6009), tetragonal (PDF No. 04-009-7947), or monoclinic (PDF No. 04-010-5719) structures of Cu_2SnS_3 (oriented in the {111}, {112}, or {200} directions, respectively). Thus, we use Raman spectroscopy to further probe the structure of the

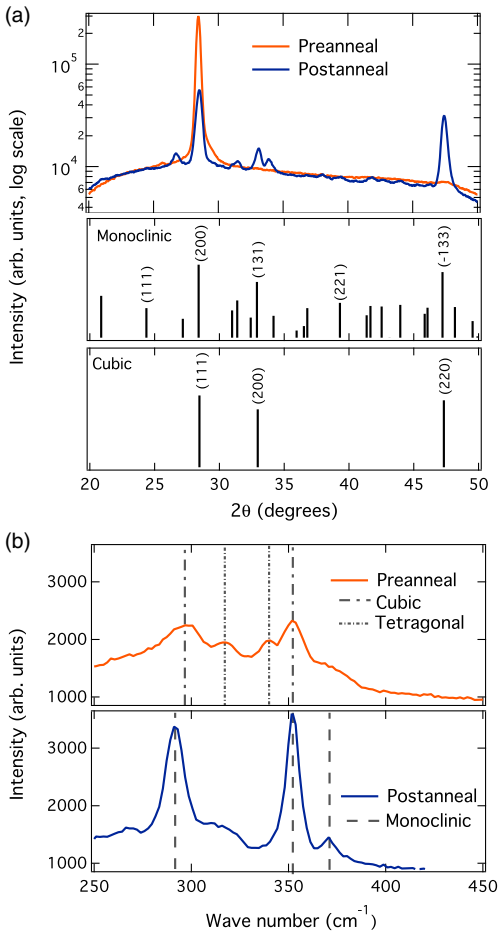

FIG. 2. (a) After annealing, the Cu_2SnS_3 films display XRD patterns corresponding to the monoclinic structure. Prior to annealing, structural determination is difficult using only one peak. (b) Raman spectroscopy allows for elucidation of the preanneal structure as a mixture of cubic and tetragonal Cu_2SnS_3. The postannealed spectrum shows peaks corresponding to the monoclinic structure, as expected from the XRD pattern.

preferentially oriented films. The preanneal Raman spectrum, shown in Fig. 2(b), shows two major peaks at 299 and 351 cm^{-1}, corresponding to the cubic Cu_2SnS_3 structure. Secondary peaks at 317 and 338 cm^{-1} could be ascribed to the tetragonal crystal structure [8]. We do not see any peaks in the 450–500 cm^{-1} range, indicating the absence of $Cu_{2-x}S$ secondary phases.

Postanneal, the XRD pattern shows peaks corresponding to the monoclinic Cu_2SnS_3 structure. The Raman spectrum has two major peaks at 290 and 351 cm^{-1}, which can be assigned to the monoclinic structure [34]. Two secondary peaks can be seen at 315 and 371 cm^{-1}. In Ref. [34], these peaks are ascribed to a $Cu_2Sn_3S_7$ secondary phase, with the corresponding cation ratio (determined by energy-dispersive x-ray spectroscopy) of $Cu/(Cu + Sn) = 0.47$. However, the cation ratio of our film, as determined by x-ray fluorescence, is $Cu/(Cu + Sn) = 0.63$, suggesting that the amounts of secondary phase present are minimal. Again, no secondary phase peaks belonging to $Cu_{2-x}S$ phases are observed.

We use XRF to measure the stoichiometry of the films before and after annealing. We do not observe any statistically significant changes in the Cu/Sn ratio of the films or changes in the film thickness. These data can be found in Table S1 in Supplemental Material [14].

Concurrent with the change in crystal structure upon annealing, we observe an improvement in the majority carrier transport. The carrier concentration decreases from $2\times10^{19}\,cm^{-3}$ for the as-deposited sample to $8.0\times10^{17}\,cm^{-3}$ after annealing. Additionally, the Hall mobility increases from 0.56 to 8.2 $cm^2/V\,s$. There are several possible explanations for the increase in hole mobility, including a reduction in grain boundary scattering due to grain growth during annealing, a reduction in ionized defect density, or a change in the effective mass between the ordered and disordered structure. Measuring the Hall mobility of the preannealed samples as a function of temperature shows the expected increase in mobility at low temperatures, suggesting that the hole transport is not grain boundary limited (see Fig. S3 [14]). When the mobility increase after annealing is considered in conjunction with the reduction in carrier concentration, it suggests that the increase in hole mobility is likely related to a reduction in the ionized defect density compared to the as-deposited sample, but a reduction in the effective mass may also play a role.

B. Terahertz spectroscopy investigation of minority carrier transport

In order to probe the minority carrier transport in the as-deposited and annealed Cu_2SnS_3, we perform OPTP spectroscopy. In contrast to the improvement observed in the hole (majority carrier) transport, the changes in electron (minority carrier) transport after annealing are less pronounced.

In the as-deposited sample, the measured reflectivity as a function of time shows two decay processes: one with a decay time of 0.3 ps, and a second with a decay time of 7 ps [see Fig. 3(a)]. When the reflectivity of the annealed Cu_2SnS_3 is compared to that of the as-deposited sample, it is clear that the 0.3-ps decay process is absent but that the 7-ps decay process remains. However, when the excitation power is lowered from 2×10^{18} to 2×10^{17} cm^{-3} (as measured in terms of excited carriers at the surface of the sample), the 0.3-ps decay process can be detected even in the annealed sample, as shown in Fig. 3(b). This suggests that the trap or defect states responsible for the 0.3-ps decay can be saturated for high carrier injection. At one sun conditions in a good absorber (100-ns carrier lifetime), there are 3×10^{16} cm^{-3} photoexcited carriers, which suggests that the 0.3-ps decay process would still dominate under normal solar cell operating conditions. We note that this decay is likely due to some kind of trapping (as opposed to a carrier lifetime as measured by techniques like time-resolved photoluminescence); the carrier lifetime within the trap could in fact be

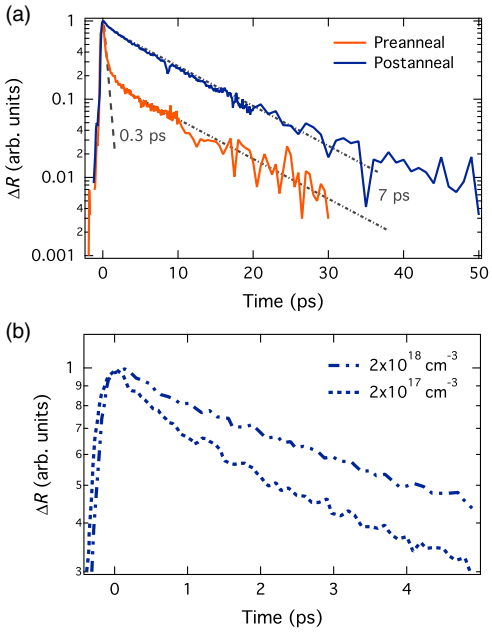

FIG. 3. (a) The as-deposited sample shows two decay processes in the measured reflectivity: a 0.3-ps decay and a 7-ps decay; the annealed sample shows only the 7-ps decay process. (b) When the excitation power is lowered, the 0.3-ps decay can be detected in the annealed sample, suggesting that this state can be saturated for high carrier injection.

much longer than this 0.3-ps decay time. However, this cannot be measured by OPTP spectroscopy, as the carriers within the traps are immobile.

For both the as-deposited and annealed samples, the imaginary component of the terahertz conductivity is negative (Fig. S4 [14]). This negative value indicates charge-carrier localization, which can be modeled by using the Drude-Smith fit for conductivity [35]. Fitting our complex conductivity data results in a determination of the relaxation scattering time τ and a constant c_1, which represents the persistence of velocity after the first scattering event. The constant c_1 can vary from -1 to 0, with $c_1 = 0$ representing Drude conductivity and $c_1 = -1$ representing complete carrier localization. For the as-deposited and annealed Cu_2SnS_3, the calculated value of c_1 is -0.91 (calculated 5–10 ps after excitation), indicating strong localization in both samples. This means that the carriers lose their initial velocity almost completely once they fall into the trap states. The relaxation scattering times are 33 and 69 fs, for the as-deposited and annealed samples, respectively.

The minority carrier dc mobility of the samples can also be calculated from the Drude-Smith model (with $\omega = 0$ for dc mobility), if the effective mass ($m^\star$) is known or approximated. Here, we approximate $m^\star$ as $0.2m_e$, the value calculated for CZTS [36]. However, it is also likely that the effective mass differs somewhat between the as-deposited and annealed samples, and this may be responsible for some of the changes in dc mobility. We calculate the minority carrier mobility to be 26 $cm^2/V\,s$ for the as-deposited Cu_2SnS_3 and 55 $cm^2/V\,s$ for the annealed sample. This factor of 2 increase in the electron mobility is related to the increase in the relaxation scattering time τ, derived from the model discussed above; alternatively, it can be explained by the decrease in effective mass due to changes in cation ordering. When we consider the extremely short decay time, we would not expect the transport in this material to be grain boundary or surface dominated, as most carriers will recombine before reaching

TABLE I. Summary of changes in crystal structure, film morphology, and majority and minority carrier transport for Cu_2SnS_3 films annealed under an SnS/argon atmosphere at 500 °C for 2 h. Significant changes are evident in the structure and morphology, and a concurrent improvement is observed in the majority carrier transport. However, the minority carrier transport is mostly unaffected by the annealing.

	Preanneal	Postanneal
Structure		
Crystal structure (XRD)	Cubic, oriented	Monoclinic
Crystal structure (Raman)	Cubic or tetragonal	Monoclinic
Crystal structure (TED)	Cubic, oriented	Monoclinic
Morphology		
Grain shape	Columnar	Equiaxed
Grain size	~50 nm	200–500 nm
Defects	High density of planar defects	Some planar and other intragrain defects
Majority-carrier transport		
Hole concentration	1×10^{19} cm^{-3}	8×10^{17} cm^{-3}
Hole mobility	0.56 $cm^2/V\,s$	8.2 $cm^2/V\,s$
Minority-carrier transport		
Electron decay times	0.3, 7 ps	0.3, 7 ps
Momentum relaxation time	33 fs	69 fs
Electron mobility	26 $cm^2/V\,s$	55 $cm^2/V\,s$
Electron localization constant	−0.91	−0.91

a grain boundary or other interface. This suggests that the increase in electron mobility is related to a reduction in the ionized defect density with annealing or a decrease in the effective mass.

C. Theoretical explanation of terahertz spectroscopy results

To interpret our finding that both the ordered and disordered samples display high degrees of electron localization, we turn to the calculated inverse participation ratio (IPR) for ordered and disordered Cu_2SnS_3. The IPR values represent the degree of charge localization: An IPR value of 1 indicates that charge is totally delocalized; an IPR value of 2 indicates that charge is localized on $\frac{1}{2}$ of the atoms present in the structure. As shown in Fig. 4(a), the ordered Cu_2SnS_3 has IPR ratios varying between 1 and 2 at the band edges (similar to values for traditional semiconductors such as Si or GaAs). In contrast, the disordered structure has high IPR values, especially at the conduction band edge, indicating a high degree of charge localization for the electrons. Both of our experimental samples, with their high degree of charge localization (c_1), are consistent with the calculated properties of the disordered sample. From the structural data (Fig. 2), the postanneal monoclinic sample is ostensibly "ordered"; however, it appears that low levels of disorder or other structural imperfections still dominate the transport properties.

If we now consider the calculated electronic DOS for ordered and disordered (i.e., clustered) Cu_2SnS_3 [Fig. 4(b)], the reason for poor minority carrier transport (Fig. 3) becomes clear. The DOS for disordered Cu_2SnS_3 [Fig. 4(b)] shows significant band tailing and a midgap state, and both of these could contribute to the picosecond electron decay times observed in the OPTP spectroscopy (Fig. 3). Additionally, the band tailing reduces the band gap of Cu_2SnS_3 (0.9–1.35 eV), ultimately reducing the final device performance.

D. Microscopy investigations

To understand how the monoclinic, ostensibly ordered sample could still exhibit properties consistent with the theoretical disordered structure (such as high c_1 values and picosecond carrier lifetimes), we use TEM to examine the microstructure of the two samples. As shown in Fig. 5(a), the as-deposited sample shows columnar grains (approximately 50 nm across) that span the thickness of the film and are strongly preferentially oriented in the ⟨111⟩ growth direction (grain boundaries are highlighted by red dashed lines). All grains have an extremely high density of planar defects (stacking faults and twins), evidenced by the dark lines within the grains, an example of which is circled in

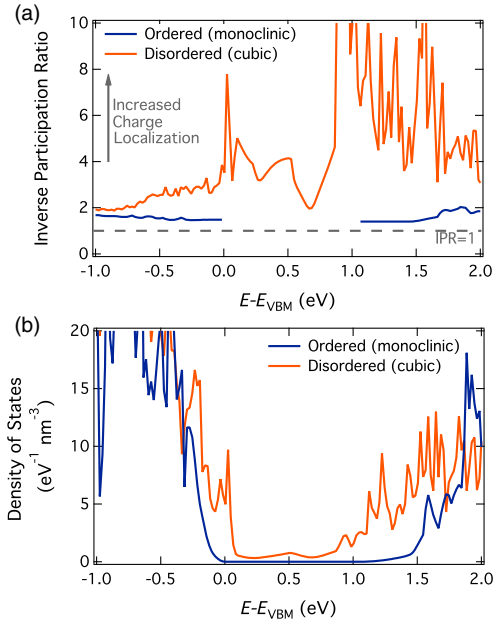

FIG. 4. (a) The calculation of the IPR for the disordered and ordered structures shows a high degree of charge localization (denoted by a high IPR value) for the disordered structure, suggesting that both of our samples exhibit disorder. Note that the ordered sample does not have states within the gap, resulting in an infinite IPR value at these energies. (b) The disordered structure results in significant band tailing and a midgap state, both of which would significantly impact the performance of a Cu_2SnS_3-based photovoltaic device.

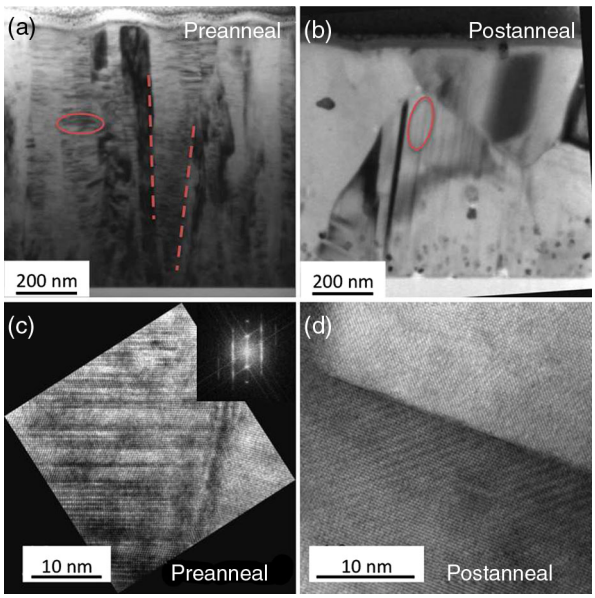

FIG. 5. (a) As-deposited films show columnar grains with an extremely high density of planar defects. (b) In the annealed films, the planar defect density is reduced in some grains but remains high in others. (c) High-resolution TEM (HRTEM) shows the planar defects in more detail, with the Fourier transform (inset) confirming the {111} nature of these defects. (d) HRTEM examination of a large number of grains does not reveal a similar high density of planar defects in the annealed films.

red. The HRTEM in Fig. 5(c) clearly shows these defects in the ⟨111⟩-oriented grains, and the streaking in the Fourier transform (inset) further confirms the presence of {111} planar defects. The transmission electron diffraction (TED) patterns [see Fig. S5(a) in Supplemental Material [14]] also confirm the zinc-blende (cubic) crystal structure, as was previously determined from the XRD pattern and Raman spectrum.

The annealed sample shows a markedly different grain structure [Fig. 5(b)]. The grains are larger (200–500 nm) and equiaxed, with no detectable preferential orientation. In this film, some of the grains still have a high density of planar defects (an example is circled in red), while most of the grains do not exhibit visible planar defects. Indeed, no evidence of stacking faults or twins is found when a number of grains are examined by using HRTEM [Fig. 5(d)]. We note that this sample is annealed for 2 h, and the 8-h anneal results in a lower carrier concentration. It is possible that the 8-h annealed sample has a higher fraction of grains without visible defects and that even longer annealing times would further reduce the density of planar defects. The TED pattern for the annealed sample is complex and is consistent with the monoclinic structure as determined by XRD and Raman [Fig. S5(b) [14]].

To understand the effects of stacking faults in Cu_2SnS_3, we define two different types of imperfections. The first we refer to as "zero-dimensional" (0D) imperfections, i.e., cation point defect disorder. This type of imperfection manifests itself in the cubic crystal structure as a result of Cu_{Sn} and Sn_{Cu} defects. However, we can also consider stacking faults to be a type of "two-dimensional" (2D) imperfection, which is also present in the cubic sample. The extremely high density of stacking faults in the as-deposited film is likely connected to the growth along the ⟨111⟩ direction, which results in an extremely low formation energy for defects at the {111} surface due to its polar character in the cubic zinc-blende-based structure. In the annealed sample, the monoclinic structure indicates a lack of 0D imperfections (cation disorder). We observe very low levels of 2D imperfections in the annealed sample. It would thus seem that this very low level of 2D imperfections still dominates the electronic transport and results in the observed charge localization and short minority carrier lifetimes that we measure in the annealed sample. Moving forward, a better understanding of both 0D and 2D imperfections will be an important research challenge that must be addressed for future improvement of Cu_2SnS_3 photovoltaic devices.

E. Implications of this work for CZTS and other disordered semiconductors

The effects of low-temperature annealing on disorder in CZTS has recently been investigated, but the resulting improvements in CZTS device efficiencies are modest [37]. This may due to a similar effect as we observe in Cu_2SnS_3, where the transport in an ostensibly ordered material (by XRD and Raman) is still dominated by a small amount of planar defects. Calculations of the inverse participation ratio for Cu_2ZnSnS_4 indicate high degrees of charge localization in the kesterite structure (see Fig. S5 [14]). The detrimental impacts of disorder in CZTS are discussed in multiple theoretical works and include band tailing, potential fluctuations on the order of 200 meV, and the formation of nanoscale compositional inhomogeneities [16,38,39]. However, we note that low-temperature disordered CZTS has an IPR distribution similar to that of the ordered kesterite; negative charge localization effects (high IPR values) are seen only in the high-temperature disordered structure, where non-ground-state motifs form in a clustered fashion (see Fig. S5 [14]) [16].

The challenge of fully eliminating disorder in CZTS has proven difficult to address experimentally, and may slow further increases in the efficiency of CZTS-based photovoltaics. Although Cu_2SnS_3 is not nearly as well studied as CZTS, the high-level similarities between these two materials suggest that Cu_2SnS_3-based devices may face similar development challenges in the future. However, the microscopic details of disorder in these two materials are quite different (i.e., motif decomposition in a single-motif structure in kesterite CZTS versus motif clustering in a two-motif structure in monoclinic Cu_2SnS_3 [16]), so this topic warrants further investigation.

Newer photovoltaic materials with potentially advantageous disorder effects are also being investigated, such as disorder-related band gap tuning in $ZnSnP_2$ [40,41]. These design ideas may offer advantages for the optical properties of the materials; however, the investigations will also need to take into account the effects of disorder on the carrier transport properties. Successful future investigations of disordered semiconductors will require the use of modeling techniques to accurately assess the electronic effects of disorder, such as those developed in Ref. [16]. Experimental quantification of the effects of disorder is equally important, using not only structural analysis but also techniques such as the terahertz spectroscopy and high-resolution TEM used in this study.

IV. CONCLUSIONS

In this study, we investigate the impacts of cation disorder on the electronic and structural properties of Cu_2SnS_3. We demonstrate the transformation from a cubic to a monoclinic crystal structure upon annealing of the Cu_2SnS_3 under an SnS atmosphere and a concurrent reduction in hole concentration by almost 2 orders of magnitude. We characterize the as-deposited (cubic or disordered) and annealed (monoclinic or ordered) samples by using optical-pump terahertz-probe spectroscopy, which detects 0.3- and 7-ps decay processes in both samples. By analyzing the complex electrical conductivity from the OPTP measurement, we determine that both samples display a high degree of charge localization. When theory

is used to calculate the charge localization in ordered and disordered Cu_2SnS_3, it suggests that charge localization is found only in the disordered structure. TEM investigations reveal low densities of planar defects in the annealed sample, which appear to still dominate the minority carrier transport.

Overall, the results presented in this work identify several challenges to the use of Cu_2SnS_3 as a photovoltaic absorber. It is possible that different synthesis techniques, such as changing the preferred growth direction, may result in a material without the planar defects exhibited in our sputtered films. However, it is also possible that the formation energy of stacking faults in Cu_2SnS_3 is particularly low, making the presence of these defects thermodynamically unavoidable. In this case, further efforts to improve upon the leading 4% efficient Cu_2SnS_3 may be hampered by the existence of 2D imperfections. As research into Cu_2SnS_3 moves forward, it will be critical to assess the charge localization and various types of imperfections and to correlate these properties with photovoltaic device performance.

ACKNOWLEDGMENTS

This work is supported by the U.S. Department of Energy, Office of Energy Efficiency and Renewable Energy, as a part of the "Rapid Development of Earth-Abundant Thin Film Solar Cells" agreement, under Contract No. DE-AC36-08GO28308 to NREL. L. L. B. is supported by the Department of Defense through the National Defense Science and Engineering Graduate Fellowship Program. T. U., R. E., and H. H. gratefully acknowledge the support of this work by the Helmholtz Association Initiative and Network Fund (HNSEI-Project). Thanks to Brenden Ortiz at the Colorado School of Mines for the synthesis of SnS and SnS_2 powders. Thanks to Lynn Gedvilas and Adam Stokes at the National Renewable Energy Laboratory for Raman spectroscopy and TEM sample preparation. Adele Tamboli at the National Renewable Energy Laboratory provided valuable discussion and input.

[1] C. A. Wolden, J. Kurtin, J. B. Baxter, I. Repins, S. E. Shaheen, J. T. Torvik, A. A. Rockett, V. M. Fthenakis, and E. S. Aydil, Photovoltaic manufacturing: Present status, future prospects, and research needs, J. Vac. Sci. Technol. A **29**, 030801 (2011).

[2] M. Woodhouse, A. Goodrich, R. Margolis, T. L. James, M. Lokanc, and R. Eggert, Supply-chain dynamics of tellurium, indium, and gallium within the context of PV manufacturing costs, IEEE J. Photovoltaics **3**, 833 (2013).

[3] G. Kavlak, J. McNerney, R. L. Jaffe, and J. E. Trancik, Metals production requirements for rapid photovoltaics deployment, Energy Environ. Sci. **8**, 1651 (2015).

[4] A. Kanai, K. Toyonaga, K. Chino, H. Katagiri, and H. Araki, Fabrication of Cu2SnS3 thin-film solar cells with power conversion efficiency of over 4%, Jpn. J. Appl. Phys. **54**, 08KC06 (2015).

[5] M. Umehara, Y. Takeda, T. Motohiro, T. Sakai, H. Awano, and R. Maekawa, $Cu_2Ge_xSn_{1-x}S_3$ ($x = 0.17$) thin-film solar cells with high conversion efficiency of 6.0%, Appl. Phys. Express **6**, 045501 (2013).

[6] P. Zawadzki, L. L. Baranowski, H. Peng, E. S. Toberer, D. S. Ginley, W. Tumas, A. Zakutayev, and S. Lany, Evaluation of photovoltaic materials within the Cu-Sn-S family, Appl. Phys. Lett. **103**, 253902 (2013).

[7] D. M. Berg, R. Djemour, L. Gutay, G. Zoppi, S. Siebentritt, and P. J. Dale, Thin film solar cells based on the ternary compound Cu_2SnS_3, Thin Solid Films **520**, 6291 (2012).

[8] P. A. Fernandes, P. M. P. Salomé, and A. F. d. Cunha, A study of ternary Cu_2SnS_3 and Cu_3SnS_4 thin films prepared by sulfurizing stacked metal precursors, J. Phys. D **43**, 215403 (2010).

[9] M. Toyonaga and H. Araki, Preparation and characterization of $Cu_2Si_xSn_{1-x}S_3$, Phys. Status Solidi C **12**, 753 (2015).

[10] Y. Dong, J. He, J. Tao, L. Sun, P. Yang, and J. Chu, Influence of different S/Se ratio on the properties of $Cu_2Sn(S_xSe_{1-x})_3$ thin films fabricated by annealing stacked metal precursors, J. Mater. Sci. **26**, 6723 (2015).

[11] J. Koike, K. Chino, N. Aihara, H. Araki, R. Nakamura, K. Jimbo, and H. Katagiri, Cu_2SnS_3 thin-film solar cells from electroplated precursors, Jpn. J. Appl. Phys. **51**, 10NC34 (2012).

[12] D. Avellaneda, M. T. S. Nair, and P. K. Nair, Cu_2SnS_3 and Cu_4SnS_4 thin films via chemical deposition for photovoltaic application, J. Electrochem. Soc. **157**, D346 (2010).

[13] K. Chino, J. Koike, S. Eguchi, H. Araki, R. Nakamura, K. Jimbo, and H. Katagiri, Preparation of Cu_2SnS_3 thin films by sulfurization of Cu/Sn stacked precursors, Jpn. J. Appl. Phys. **51**, 10NC35 (2012).

[14] See Supplemental Material at http://link.aps.org/supplemental/10.1103/PhysRevApplied.4.044017 for additional methods and results.

[15] Y. T. Zhai, S. Chen, J. H. Yang, H. J. Xiang, X. G. Gong, A. Walsh, J. Kang, and S. H. Wei, Structural diversity and electronic properties of Cu_2SnX_3 (X = S, Se): A first-principles investigation, Phys. Rev. B **84**, 075213 (2011).

[16] P. Zawadzki, A. Zakutayev, and S. Lany, Entropy-Driven Clustering in Tetrahedrally Bonded Multinary Materials, Phys. Rev. Applied **3**, 034007 (2015).

[17] U. Chalapathi, Y. Jayasree, S. Uthanna, and V. Sundara Raja, Effect of annealing temperature on the properties of spray deposited Cu_2SnS_3 thin films, Phys. Status Solidi (a) **210**, 2384 (2013).

[18] D. Tiwari, T. K. Chaudhuri, and T. Shripathi, Electrical transport in layer-by-layer solution deposited Cu_2SnS_3 films: Effect of thickness and annealing temperature, Appl. Surf. Sci. **297**, 158 (2014).

[19] N. Aihara, H. Araki, A. Takeuchi, K. Jimbo, and H. Katagiri, Fabrication of Cu_2SnS_3 thin films by sulfurization of evaporated Cu-Sn precursors for solar cells, Phys. Status Solidi (c) **10**, 1086 (2013).

[20] Z. Su, K. Sun, Z. Han, F. Liu, Y. Lai, J. Li, and Y. Liu, Fabrication of ternary Cu–Sn–S sulfides by a modified

successive ionic layer adsorption and reaction (SILAR) method, J. Mater. Chem. **22**, 16346 (2012).

[21] L. L. Baranowski, P. Zawadzki, S. Christensen, D. Nordlund, S. Lany, A. C. Tamboli, L. Gedvilas, D. S. Ginley, W. Tumas, E. S. Toberer, and A. Zakutayev, Control of doping in Cu_2SnS_3 through defects and alloying, Chem. Mater. **26**, 4951 (2014).

[22] M. L. Green, I. Takeuchi, and J. R. Hattrick-Simpers, Applications of high throughput (combinatorial) methodologies to electronic, magnetic, optical, and energy-related materials, J. Appl. Phys. **113**, 231101 (2013).

[23] A. Zakutayev, V. Stevanovic, and S. Lany, Non-equilibrium alloying controls optoelectronic properties in Cu_2O thin films for photovoltaic absorber applications, Appl. Phys. Lett. **106**, 123903 (2015).

[24] A. W. Welch, P. Zawadzki, S. Lany, C. A. Wolden, and A. Zakutayev, Self-regulated growth and tunable properties of $CuSbS_2$ solar absorbers, Sol. Energy Mater. Sol. Cells **132**, 499 (2015).

[25] C. M. Caskey, R. M. Richards, D. S. Ginley, and A. Zakutayev, Thin film synthesis and properties of copper nitride, a metastable semiconductor, Mater. Horiz. **1**, 424 (2014).

[26] C. Strothkamper, K. Schwarzburg, R. Schutz, R. Eichberger, and A. Bartelt, Multiple-trapping governed electron transport and charge separation in ZnO/In_2S_3 core/shell nanorod heterojunctions, J. Phys. Chem. C **116**, 1165 (2012).

[27] C. C. Katsidis and D. I. Siapkas, General transfer-matrix method for optical multilayer systems with coherent, partially coherent, and incoherent interference, Appl. Opt. **41**, 3978 (2002).

[28] C. Strothkamper, A. Bartelt, R. Eichberger, C. Kaufmann, and T. Unold, Microscopic mobilities and cooling dynamics of photoexcited carriers in polycrystalline $CuInSe_2$, Phys. Rev. B **89**, 115204 (2014).

[29] G. Kresse and D. Joubert, From ultrasoft pseudopotentials to the projector augmented-wave method, Phys. Rev. B **59**, 1758 (1999).

[30] J. Heyd, G. E. Scuseria, and M. Ernzerhof, Hybrid functionals based on a screened Coulomb potential, J. Chem. Phys. **118**, 8207 (2003).

[31] S. L. Dudarev, G. A. Botton, S. Y. Savrasov, C. J. Humphreys, and A. P. Sutton, Electron-energy-loss spectra and the structural stability of nickel oxide: An LSDA + U study, Phys. Rev. B **57**, 1505 (1998).

[32] J. P. Perdew, K. Burke, and M. Ernzerhof, Generalized Gradient Approximation Made Simple, Phys. Rev. Lett. **77**, 3865 (1996).

[33] J. P. Perdew, K. Burke, and M. Ernzerhof, Erratum: Generalized Gradient Approach Made Simple, Phys. Rev. Lett. **78**, 1396(E) (1997).

[34] D. M. Berg, R. Djemour, L. Gutay, S. Siebentritt, and P. J. Dale, Raman analysis of monoclinic Cu_2SnS_3 thin films, Appl. Phys. Lett. **100**, 192103 (2012).

[35] N. V. Smith, Classical generalization of the Drude formula for the optical conductivity, Phys. Rev. B **64**, 155106 (2001).

[36] H. R. Liu, S. Chen, Y. T. Zhai, H. J. Xiang, X. G. Gong, and S. H. Wei, First-principles study on the effective masses of zinc-blend-derived Cu_2Zn-IV-VI_4 (IV = Sn, Ge, Si and VI = S, Se), J. Appl. Phys. **112**, 093717 (2012).

[37] S. C. Siah, R. Jaramillo, R. Chakraborty, P. T. Erslev, C. Sun, T. Weng, M. F. Toney, G. Teeter, and T. Buonassisi, X-ray absorption spectroscopy study of structure and stability of disordered $(Cu_2SnS_3)_{1-x}(ZnS)_x$ alloys, IEEE J. Photovoltaics **5**, 372 (2015).

[38] T. Gokmen, O. Gunawan, and D. B. Mitzi, Semi-empirical device model for $Cu_2ZnSn(S, Se)_4$ solar cells, Appl. Phys. Lett. **105**, 033903 (2014).

[39] P. Zawadzki and S. Lany (to be published).

[40] G. A. Seryogin, S. A. Nikishin, H. Temkin, A. M. Mintairov, J. L. Merz, and M. Holtz, Order-disorder transition in epitaxial $ZnSnP_2$, Appl. Phys. Lett. **74**, 2128 (1999).

[41] D. O. Scanlon and A. Walsh, Bandgap engineering of $ZnSnP_2$ for high-efficiency solar cells, Appl. Phys. Lett. **100**, 251911 (2012).